

# High-entropy polymer produces a giant electrocaloric effect at low fields

<https://doi.org/10.1038/s41586-021-04189-5>

Received: 16 May 2021

Accepted: 26 October 2021

Published online: 22 December 2021

 Check for updates

Xiaoshi Qian<sup>1,2,12</sup>, Donglin Han<sup>1,12</sup>, Lirong Zheng<sup>3,12</sup>, Jie Chen<sup>4,12</sup>, Madhusudan Tyagi<sup>5,6</sup>, Qiang Li<sup>1</sup>, Feihong Du<sup>1</sup>, Shanyu Zheng<sup>1</sup>, Xingyi Huang<sup>4</sup>, Shihai Zhang<sup>7</sup>, Junye Shi<sup>1</sup>, Houbing Huang<sup>8</sup>, Xiaoming Shi<sup>8</sup>, Jiangping Chen<sup>1</sup>, Hancheng Qin<sup>9</sup>, Jerzy Bernholc<sup>9</sup>, Xin Chen<sup>10</sup>, Long-Qing Chen<sup>10</sup>, Liang Hong<sup>3</sup> & Q. M. Zhang<sup>11</sup>

More than a decade of research on the electrocaloric (EC) effect has resulted in EC materials and EC multilayer chips that satisfy a minimum EC temperature change of 5 K required for caloric heat pumps<sup>1–3</sup>. However, these EC temperature changes are generated through the application of high electric fields<sup>4–8</sup> (close to their dielectric breakdown strengths), which result in rapid degradation and fatigue of EC performance. Here we report a class of EC polymer that exhibits an EC entropy change of  $37.5 \text{ J kg}^{-1} \text{ K}^{-1}$  and a temperature change of 7.5 K under  $50 \text{ MV m}^{-1}$ , a 275% enhancement over the state-of-the-art EC polymers under the same field strength. We show that converting a small number of the chlorofluoroethylene groups in poly(vinylidene fluoride-trifluoroethylene-chlorofluoroethylene) terpolymer into covalent double bonds markedly increases the number of the polar entities and enhances the polar–nonpolar interfacial areas of the polymer. The polar phases in the polymer adopt a loosely correlated, high-entropy state with a low energy barrier for electric-field-induced switching. The polymer maintains performance for more than one million cycles at the low fields necessary for practical EC cooling applications, suggesting that this strategy may yield materials suitable for use in caloric heat pumps.

The refrigerant gases used in the conventional cooling technology based on the vapour compression cycle are one of the leading causes of global warming<sup>9</sup>, and cooling is an energy-intensive activity, consuming more than 20% of the electricity generated in the world<sup>2</sup>. Solid-state cooling technologies based on caloric effects present an attractive alternative to the vapour compression cycle owing to their zero greenhouse gas emission and the promise of higher operating efficiency. A caloric material generates a reversible temperature and entropy change through the application of an applied field including electric fields (EC), magnetic fields (magnetocaloric)<sup>10</sup> or mechanical stresses (elastocaloric, barocaloric and twistocaloric effect)<sup>11–13</sup>. EC heat pumps of various geometries (linear<sup>4</sup>, rotary<sup>14</sup> and cascaded<sup>8</sup>), and using different strategies of heat transfer (solid–fluid<sup>6</sup> and solid–solid<sup>5</sup>), charge recovery<sup>15</sup> and active regeneration<sup>7</sup>, have been reported, and many approaches, including composites and blends, have been investigated to improve the EC performance<sup>16</sup> of the working material<sup>17</sup>.

Ceramic multilayer chips (MLCs) that exhibit directly measured  $\Delta T > 5.5 \text{ K}$  (under  $29 \text{ MV m}^{-1}$ )<sup>3</sup>, and polymeric thick films that exhibit  $\Delta S = 76 \text{ J kg}^{-1} \text{ K}^{-1}$  (under  $150 \text{ MV m}^{-1}$ , corresponding to  $\Delta T \approx 15 \text{ K}$ )<sup>18</sup> have

been reported. However, high EC effects (ECEs) do not necessarily translate into practical EC heat pumps owing to high-field-induced fatigue. This means that reported EC devices operate far below the maximum  $\Delta T$  of their working bodies: 2.2 K for both ceramic and polymeric MLCs<sup>4,6,7</sup>.

## Defect-modified high-entropy EC polymer

To induce a large ECE under low electric fields, we chose poly(vinylidene fluoride<sub>65</sub>-trifluoroethylene<sub>35</sub>-chlorofluoroethylene<sub>7</sub>) (P(VDF<sub>65</sub>-TrFE<sub>35</sub>-CFE<sub>7</sub>)) terpolymer (we kept the sum of the first two monomers as 100%) as the base polymer for our study because this polymer generates the highest entropy change among EC materials reported,  $\Delta S > 200 \text{ J kg}^{-1} \text{ K}^{-1}$ , under fields  $> 250 \text{ MV m}^{-1}$  (ref. <sup>19</sup>). The bulky CFE groups, serving as a molecular defect, destabilize the bulky and highly correlated polar domain of P(VDF<sub>65</sub>-TrFE<sub>35</sub>) mol%, and dramatically enhance the ECE at room temperature<sup>18</sup>.

However, a low-field ECE of the terpolymer is difficult to enhance further by tuning the CFE content. When the fraction of CFE is low,

<sup>1</sup>Institute of Refrigeration and Cryogenics, Interdisciplinary Research Centre for Metamaterials and Intelligent Systems, State Key Laboratory of Mechanical System and Vibration, and MOE Key Laboratory for Power Machinery and Engineering, School of Mechanical Engineering, Shanghai Jiao Tong University, Shanghai, China. <sup>2</sup>Shanghai Jiao Tong University Jiangsu ZhongGuanCun Research Institute, Liyang, Jiangsu, China. <sup>3</sup>School of Physics and Astronomy, Institute of Natural Sciences, Shanghai National Center for Applied Mathematics (SJTU Center) and MOE-LSC, Shanghai Jiao Tong University, Shanghai, China. <sup>4</sup>Frontiers Science Center for Transformative Molecules, Department of Polymer Science and Engineering, Shanghai Key Laboratory of Electrical Insulation and Thermal Ageing, State Key Laboratory of Metal Matrix Composites, Shanghai Jiao Tong University, Shanghai, China. <sup>5</sup>NIST Center for Neutron Research, National Institute of Standards and Technology (NIST), Gaithersburg, MD, USA. <sup>6</sup>Department of Materials Science and Engineering, University of Maryland, College Park, MD, USA. <sup>7</sup>PolyK Technologies, State College, PA, USA. <sup>8</sup>School of Materials Science and Engineering and Advanced Research Institute of Multidisciplinary Science, Beijing Institute of Technology, Beijing, China. <sup>9</sup>Department of Physics, North Carolina State University, Raleigh, NC, USA. <sup>10</sup>Department of Materials Science and Engineering, Pennsylvania State University, University Park, PA, USA. <sup>11</sup>School of Electrical Engineering and Computer Science and Department of Mechanical Engineering, The Pennsylvania State University, University Park, PA, USA. <sup>12</sup>These authors contributed equally: Xiaoshi Qian, Donglin Han, Lirong Zheng, Jie Chen. <sup>✉</sup>e-mail: xsqian@sjtu.edu.cn; xyhuang@sjtu.edu.cn; hbhuang@bit.edu.cn; hongl3liang@sjtu.edu.cn

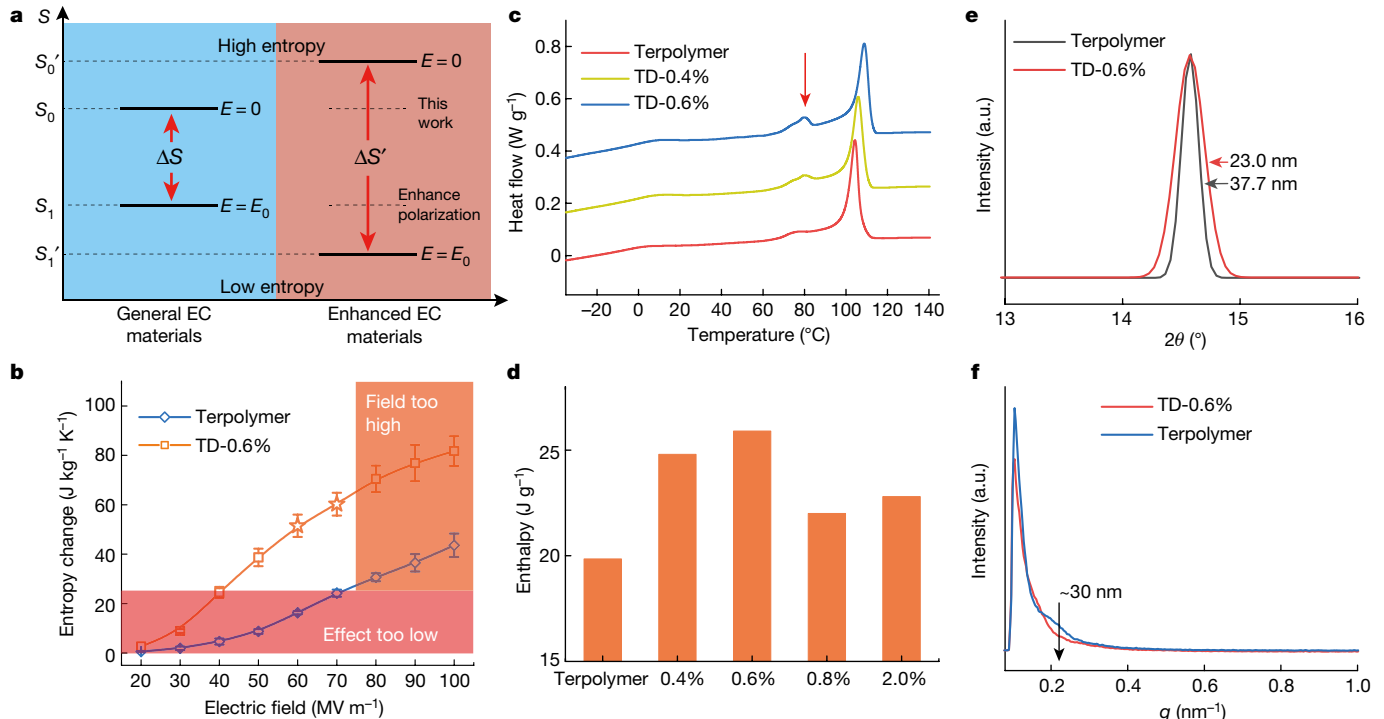


**Fig. 1 | Entropy-enhanced polymers exhibit giant ECEs under low fields.**

**a**, Principle for achieving a larger ECE at a certain electric field. ECEs can be greatly enhanced by reaching a low-entropy state at  $E = E_0$  (enhancing polarization, shown as downward arrow) and tuning to a high-entropy state at  $E = 0$  (this work). **b**, TD-0.6% polymer exhibits greatly enhanced entropy changes of  $>25 \text{ J kg}^{-1} \text{ K}^{-1}$  under  $50\text{--}70 \text{ MV m}^{-1}$ , which is within the window of technical viability

( $n \geq 3$ , points are centred on the mean and the bars indicate the s.d., each sample in the EC heat flux measurement was verified by independent measurements by an infrared camera, see Supplementary Sections 1.6 and 1.7). **c, d**, Latent heat during crystallization (**c**) and integrated enthalpy of crystallization (**d**) of the base terpolymer and the TD series. **e, f**, WAXD (amorphous region subtracted) (**e**) and SAXS (**f**) of the base terpolymer and TD-0.6%.

the terpolymer still maintains macroscopic polar domains that cause undesirable irreversibility, and possess low dipolar entropy. On the other hand, an over-incorporation of the CFE groups significantly diminishes the crystallinity of the polymer<sup>20</sup>, thus reducing ECE as well. Therefore, it is essential to incorporate additional defects in the polymer to enhance the dipolar disordering at zero field without sacrificing its crystallinity.

Defect-induced disordering has been utilized to manipulate material properties by providing nucleation sites<sup>21</sup>, increasing interface areas<sup>22</sup>, lowering the energy barrier of transitions<sup>23</sup>, tuning the intermolecular interactions<sup>24</sup> and so on. We note that material responses of ferroelectrics can be tuned over a wide range by material compositions and defect-induced interfaces<sup>25</sup>. It has been reported that interface effects make a significant contribution to the piezoelectric response of PVDF-based ferroelectric polymers<sup>26</sup>.

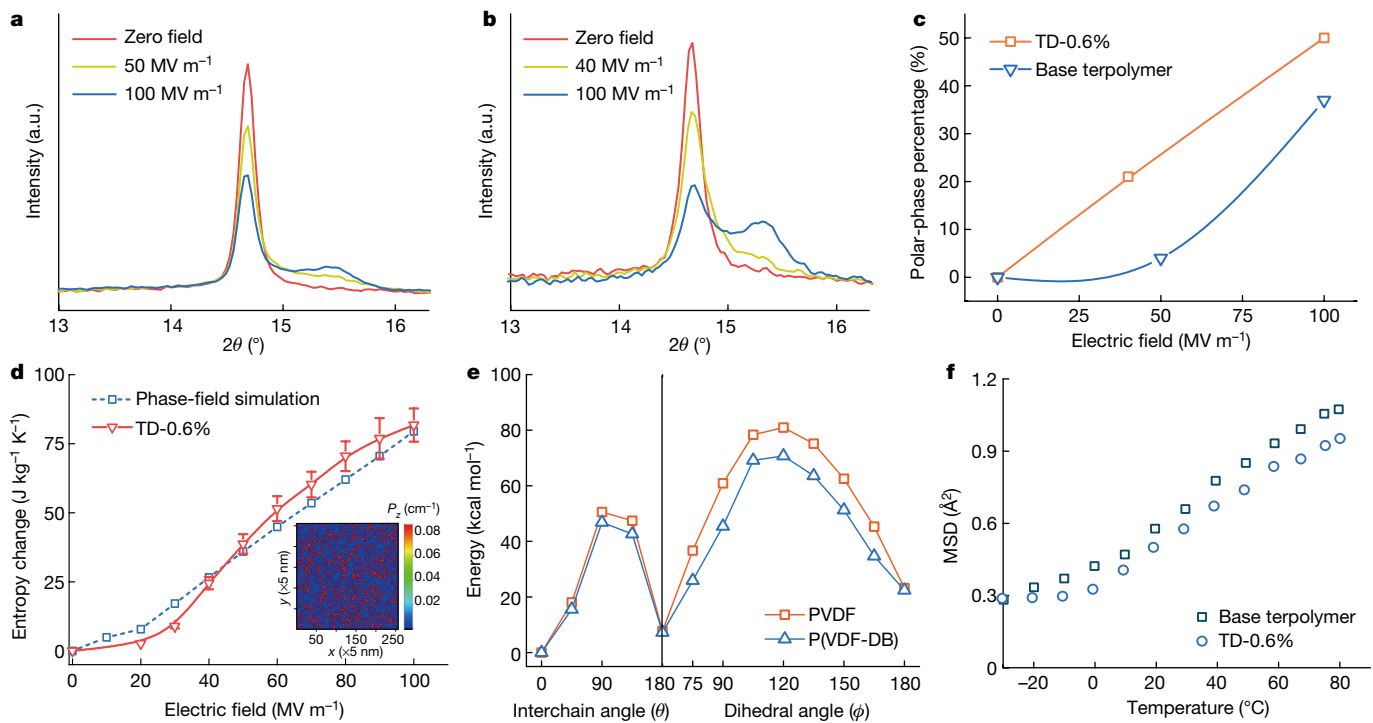
Hence, we set a goal to reduce the concentration of CFE and leave a small amount of double bonds (DBs) as an additional factor of modulation (confirmed by NMR spectroscopy, energy-dispersive X-ray spectroscopy, Raman spectroscopy and Fourier-transform infrared spectroscopy; see Supplementary Section 1) to enhance the polar entropy of the polymer (Fig. 1a). The material was treated with a widely reported de-hydrochlorination method<sup>27</sup> (Methods). The method has been applied to many PVDF-based polymers, including P(VDF-TrFE-CTFE) (ref. <sup>28</sup>), which exhibited quite different dielectric and ferroelectric properties compared with the state-of-the-art EC polymer P(VDF-TrFE-CFE) adopted here.

Figure 1b presents  $\Delta S$  of the resulting P(VDF<sub>65</sub>-TrFE<sub>35</sub>-CFE<sub>7-x</sub>-DB<sub>x</sub>) with  $x = 0.6 \text{ mol\%}$  (referred to as TD-0.6% in this work) and its comparison with the base terpolymer. The data reveal a great enhancement of EC response at all fields measured, especially at ultralow electric fields. The effect is far above the 5-K threshold under a low field for the polymer (Extended Data Fig. 1) even when the inactive materials in MLCs were

considered (Extended Data Fig. 2). In Extended Data Fig. 3, we present  $\Delta S$  of the modified polymers at different DB mol% versus the applied field, which reveals an enhanced ECE in all of the DB compositions studied. The EC enhancement of TD-2% at ultralow fields is small, and hence no study was conducted beyond 2 mol% DBs.

By slightly reducing the content of CFE by 0.6 mol%, the crystallinity of the polymer was enhanced by 25%, as observed from the differential scanning calorimetry (DSC) results of the melting enthalpy enhancement from 25.7 for the base terpolymer to  $29.7 \text{ J g}^{-1}$  for the TD-0.6% (Extended Data Fig. 4), with a corresponding crystallization enthalpy enhancement from 19.9 to  $25.9 \text{ J g}^{-1}$  (Fig. 1c, d), which was expected when the CFE content was reduced. With a lower content of CFE groups as molecular defects, we normally expect a concurrently increased crystallinity and crystal size. Instead, we noticed that the average crystal size in the TD-0.6% was reduced to 23 nm from 37 nm of the base terpolymer (Fig. 1e).

The enhanced crystallinity and reduced size of crystalline structures imply that the material hosts a substantially increased number of crystallites and regions of crystalline–amorphous interfaces. From the DSC data, we observed a strong second exothermic peak following the crystallization in the DSC cooling scan data of TD-0.6% (red arrow in Fig. 1c), indicating that additional crystallites were formed right below the temperature of crystallization. The DB-induced defects may serve as nucleation sites to facilitate the formation of small crystallites that would be separated and localized in space. The resulting polymer would self-organize into a highly disordered state with an enhanced configurational entropy. These results were supported by small-angle X-ray scattering (SAXS) data that suggested the suppression of long-range ordering in the terpolymer, after 0.6 mol% CFE groups were reduced to DBs (Fig. 1f). The disordering suggested by the SAXS data can be visualized on cryo electron micrographs, which indicate that the DB-modified polymer has a finer and more



**Fig. 2 | Structural properties of the modified EC polymers and their base terpolymer.** **a, b,** In situ WAXD of P(VDF-TrFE-CFE) (**a**) and the entropy-enhanced TD-0.6% (**b**). **c,** Fraction of polar-phase changes as a function of the electric field. **d,** Experimental and phase-field simulation results of the field-dependent ECE ( $n \geq 3$ , points are centred on the mean and the bars indicate the s.d., each sample in the EC heat flux measurement was verified

by independent measurements by an infrared camera, see Supplementary Sections 1.6 and 1.7). The inset shows the spatial distribution of the polar crystalline phases, generated in the phase-field model, when the external field is  $50 \text{ MV m}^{-1}$ . **e,** Energies along the transformation pathway from the  $\alpha$  to the  $\beta$  phase, for pure PVDF and P(VDF-DB) 99.5/0.5 mol%. **f,** The MSD of the base terpolymer and the TD-0.6%.

randomized texture than that of the base terpolymer (Supplementary Section 1.8). When the significantly increased polar entities arrange in a disordered manner, we expect a greatly enhanced dipolar entropy at zero field.

A highly disordered crystalline structure alone may not imply a large ECE at low field, which would require an efficient transition from the high-entropy state (nonpolar) to a low-entropy (polar) state. Figure 2a, b presents in situ wide-angle X-ray diffraction (WAXD) data, from which we observed that the TD-0.6% exhibits a significantly enhanced phase transformation compared with that of the base terpolymer. Quantitatively, the TD-0.6% showed that  $>20\%$  volume fraction of the nonpolar phase transformed into the polar  $\beta$  phase when the field was increased to  $40 \text{ MV m}^{-1}$ , whereas for the base terpolymer only  $4\%$  volume fraction was converted even under a higher field of  $50 \text{ MV m}^{-1}$  (that is, one-fifth of that of the TD-0.6%; see Supplementary Table 1 and Fig. 2c).

In general, energy barriers for switching from nonpolar to polar phases should be much lower for smaller crystallites and interfacial regions owing to reduced constraints. To understand its impact on ECE on a relatively large scale, we developed a phase-field model for the high-entropy EC polymer, in which the field-dependent crystalline structure was constructed according to the in situ WAXD data. Based on the well-established time-dependent Ginzburg–Landau and stress equilibrium equations, the computational ECE is consistent with the experimental results (Fig. 2d and Supplementary Section 2). On the molecular scale, we constructed a density functional theory (DFT) framework to qualitatively evaluate the contribution of DBs along the transformation pathway from the nonpolar  $\alpha$  to the  $\beta$  phase (Supplementary Section 3). For simplicity, only VDF monomers with/without DBs were considered. The results indicated that the DBs alone reduced the energy barrier for the  $\alpha$ -to- $\beta$  phase transition by  $10 \text{ kcal mol}^{-1}$  (Fig. 2e). Moreover, we also conducted a molecular mechanics simulation to study the conformational transition of

the base terpolymer. The results show that the energy barrier for the transition from *trans-trans* (TT) to *trans-gauche/trans-gauche'* (TG/TG') is around  $6 \text{ kcal mol}^{-1}$  (corresponding to a timescale  $\sim 100 \text{ ns}$ ; Extended Data Fig. 5), quantitatively agreeing with the reported value by NMR spectroscopy (ref. <sup>29</sup>). Importantly, the addition of DBs will significantly reduce this intrachain conformational energy barrier, which will facilitate the  $\alpha$ -to- $\beta$  phase transition, consistent with the results derived from DFT (Fig. 2e).

While the polymer chain of TD-0.6% rotates and switches more easily than the base terpolymer, a simple tensile stress test suggests an enhanced elastic modulus for the DB-modified terpolymer (Supplementary Fig. 4). We performed elastic neutron scattering on these polymers to probe atomic fluctuation of hydrogen atoms at a short timescale ( $\sim 1 \text{ ns}$ ), much shorter than that of the chain rotation,  $\sim 100 \text{ ns}$ . The mean square displacements (MSDs) of the TD-0.6% are smaller than those of the base terpolymer in the entire temperature range from  $-20^\circ\text{C}$  to  $80^\circ\text{C}$  (Fig. 2f), indicating a greater modulus for the TD-0.6% sample<sup>30</sup>, consistent with the tensile stress measurement. The reduced atomic fluctuation could arise from the enhanced crystallinity of the TD-0.6% polymer, as the movement of hydrogen atoms would be more restrained in a closely packed crystalline phase than in the amorphous regions. The above results therefore depict sophisticated polymer dynamics that enables a high-entropy state in a mechanically rigid polymer with lower intrachain conformational energy barriers, leading to giant ECE at low fields.

## Dielectric responses

We characterized the dielectric response of the TD series to corroborate the polymeric, high-entropy state and the giant low-field ECE. The temperature-dependent permittivity revealed an outstanding feature as the terpolymer is being converted to the TD series with increasing

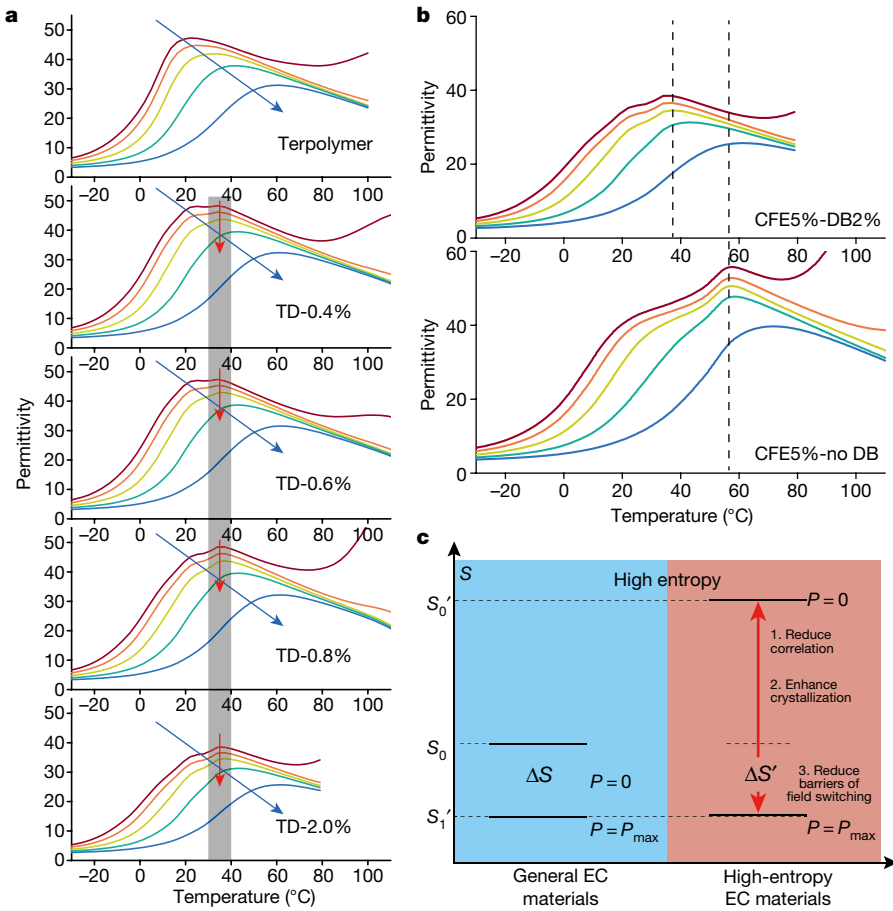


**Fig. 3 | Dielectric properties of the modified EC polymer and its base terpolymer.** **a**, Temperature-dependent permittivity of the base terpolymer and the TD series with different mole percentages of CFE reduction. The blue and red arrows indicate the dielectric behaviour of relaxor and polar phases, respectively. **b**, Temperature-dependent permittivity of P(VDF-TrFE-CFE) with and without the DBs. **c**, The enhanced ECE in the TD-0.6% polymer under

50 MV m<sup>-1</sup>. Compared with the base terpolymer showing a low-entropy state at  $P = 0$ , the TD-0.6% polymer exhibited a high-entropy,  $P = 0$  state, and high polar-phase content at 50 MV m<sup>-1</sup>. The high-entropy EC polymer possesses a high crystallinity with less polar correlation, and a reduced barrier for field-induced switching.

DB mol% (Fig. 3a). That is, in addition to a broad dielectric peak that progressively moves to high temperature with increasing frequency (a feature of a ferroelectric relaxor, indicated by the blue arrows in Fig. 3a), a weak and relatively sharp dielectric peak appeared around 36 °C, and the peak position seems frequency-independent (red arrows in Fig. 3a). The appearance of such a peak suggests the presence of a weak polar phase while the CFE content is reduced. Interestingly, the frequency-independent peaks in the TD series were strongly pinned at 36 °C with reduced CFE content. In a conventional dielectric system, the dielectric peaks are expected to move to high temperature with increased polar phases that would form highly correlated polar domains, as shown in Extended Data Fig. 6 for ferroelectric/relaxor polymer blends.

We explored the temperature-pinning effect by comparing the dielectric performances of a terpolymer P(VDF<sub>65</sub>-TrFE<sub>35</sub>-CFE<sub>5</sub>) with/without DB content. As shown in Fig. 3b, the terpolymer exhibited frequency-independent peaks located at 55 °C, indicating the existence of strongly correlated polar phases as the CFE content decreases from 7 to 5 mol%. The counterintuitive pinning effect at 36 °C of the TD-2% (P(VDF<sub>65</sub>-TrFE<sub>35</sub>-CFE<sub>5</sub>-DB<sub>2</sub>)) suggested that DB-induced defects prevent the formation of bulky and strongly correlated polar regions, which were especially valuable considering that the overall crystallinity is increasing. The large number of newly formed, small-sized polar entities adopted a loosely correlated, high-entropy state, as suggested by DSC and XRD results.

The polarization–electric field ( $P$ – $E$ ) loops were measured and are presented in Extended Data Fig. 7. The TD-0.6% films display slim  $P$ – $E$  loops but show lower maximum polarization,  $P_{\max}$ , than the base terpolymer, despite having a much larger ECE than the base terpolymer. This observation is unique as most research reports enhanced ECE with increased polarization and long-range ordering<sup>28</sup>. According to the Landau–Devonshire phenomenological theory

$$\Delta S \cong -\frac{1}{2}\beta(P^2(E_h) - P^2(E_l)) \quad (1)$$

where  $E_l = 0$  and  $\Delta S \cong -\frac{1}{2}\beta P^2(E_h)$  with  $\beta = \ln(\Omega)/(\varepsilon_0\Theta)$  (ref. <sup>31</sup>). Here,  $E_l$  is the low electric field and  $E_h$  the high electric field,  $\varepsilon_0$  is the permittivity of vacuum, and  $\Theta$  is an effective Curie constant, which is directly related to the polar correlation in dielectrics. The results indicated that, a large  $\Omega$ , which corresponds to the number of polar entities accessible by dipoles, and a weak polar correlation  $\Theta$  will result in a large  $\beta$  (Extended Data Fig. 7) and giant ECE at low fields.

Taken together, the dielectric properties suggest that the terpolymer modified by reducing a small amount of CFE groups to DBs possesses a much higher dipolar entropy and much lower barriers for the field-induced transition than that of the base terpolymer, which results in a giant ECE at low electric fields, as summarized in Fig. 3c.

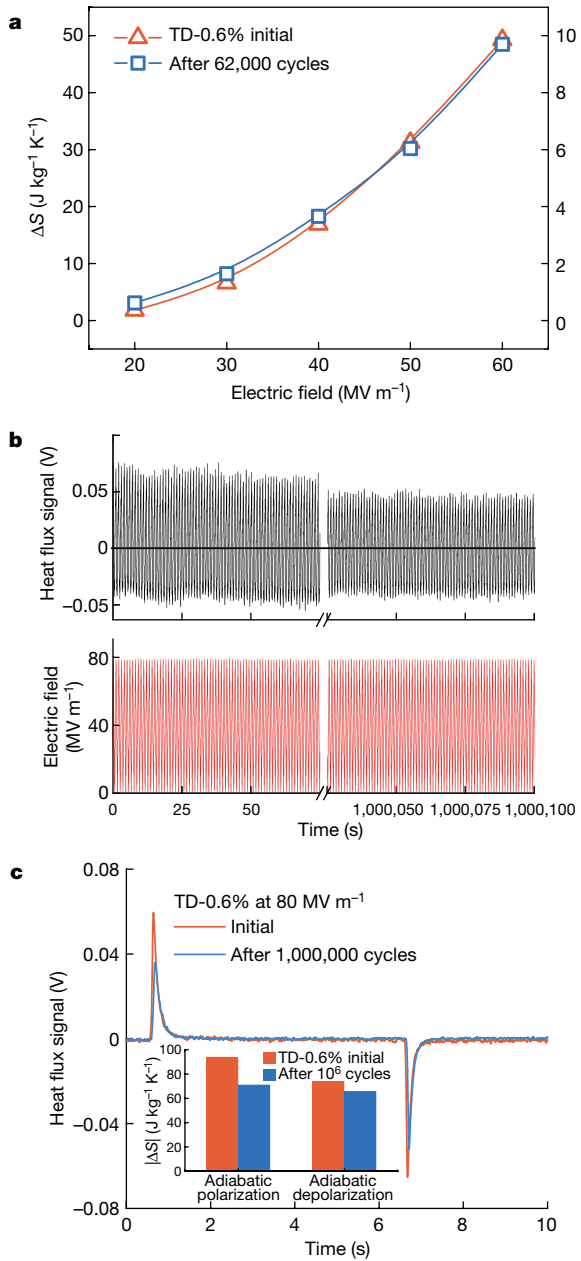


**Fig. 4 | High-entropy EC polymer and its impact on device performances.** **a**, Field-dependent ECE of TD-0.6% tested initially and after 62,000 cycles.  $\Delta T_{\text{ad}}$  refers to the adiabatic temperature change derived from the EC heat flux measurement. **b**, Directly recorded heat flux (top panel) and the driving field (bottom panel) in the first 100 and the last 100 cycles during a long-term, million-cycle measurement of ECE. **c**, Comparison of the recorded EC-induced heat flux between the initial cycle and the millionth cycle. The inset summarizes the EC-induced entropy change during adiabatic polarization and depolarization, before and after 1 million cycles.

## Material impact on device performance

We characterized the fatigue performance of TD-0.6% under different electric fields and compare it with the base terpolymer under the same cycling conditions. After 61,200 cycles, the ECE of the terpolymer was reduced by 60%, from  $23.5 \text{ J kg}^{-1} \text{K}^{-1}$  to  $9 \text{ J kg}^{-1} \text{K}^{-1}$  (Extended Data Fig. 8), which can be explained by the growth of nanodomains on repeated electric poling<sup>32</sup>. By contrast, the TD-0.6 mol% exhibited less than 10% reduction in the ECE after one million cycles, as shown in Fig. 4a, b. Under  $50 \text{ MV m}^{-1}$ , the TD-0.6% films exhibit very little fatigue of EC response (Extended Data Fig. 9a).

TD-0.6% samples were then cycled continuously in-house without specific environmental controls for 23 days (0.5 Hz) or 11 days (1 Hz). After 1 million cycles under  $80 \text{ MV m}^{-1}$ , the high-entropy EC polymer film maintained heat absorption at 90% of the initial state (Fig. 4c). To achieve the same amount of cooling, the base terpolymer required  $150 \text{ MV m}^{-1}$ , and the film quickly underwent several partial breakdowns and failed after only 50 cycles (Extended Data Fig. 9b). In addition, we observed that the heat ejection ( $Q_H$ ) and absorption ( $Q_C$ ) were more balanced during the cycling (that is,  $(Q_H - Q_C)/Q_H$  reduced from 21% to 7% as shown in Fig. 4c), indicating a smaller irreversible heat loss of the TD-0.6%, and the total hysteresis heat of TD-0.6% was merely 10% of that of the base terpolymer (Extended Data Fig. 10). The fatigue-resistant behaviour and reduced heat loss are both desirable for an EC cooling device. We constructed a computational model of a previously reported EC device to further illustrate the impact of the high-entropy EC polymer. The device operating TD-0.6% achieved a zero- $T_{\text{span}}$  cooling power density of  $5.2 \text{ kW kg}^{-1}$ , a zero-power  $T_{\text{span}}$  of  $63 \text{ K}$  under  $50 \text{ MV m}^{-1}$  and the highest COP of 11.4 (~80% of the Carnot coefficient of performance; see Supplementary Section 4).

## Online content

Any methods, additional references, Nature Research reporting summaries, source data, extended data, supplementary information, acknowledgements, peer review information; details of author contributions and competing interests; and statements of data and code availability are available at <https://doi.org/10.1038/s41586-021-04189-5>.

1. Qian, S. et al. Not-in-kind cooling technologies: a quantitative comparison of refrigerants and system performance. *Int. J. Refrig.* **62**, 177–192 (2016).
2. Shi, J. et al. Electrocaloric cooling materials and devices for zero-global-warming-potential, high-efficiency refrigeration. *Joule* **3**, 1200–1225 (2019).
3. Nair, B. et al. Large electrocaloric effects in oxide multilayer capacitors over a wide temperature range. *Nature* **575**, 468–472 (2019).
4. Gu, H. et al. A chip scale electrocaloric effect based cooling device. *Appl. Phys. Lett.* **102**, 122904 (2013).
5. Ma, R. et al. Highly efficient electrocaloric cooling with electrostatic actuation. *Science* **357**, 1130–1134 (2017).
6. Torelló, A. et al. Giant temperature span in electrocaloric regenerator. *Science* **370**, 125–129 (2020).
7. Wang, Y. et al. A high-performance solid-state electrocaloric cooling system. *Science* **370**, 129–133 (2020).
8. Meng, Y. et al. A cascade electrocaloric cooling device for large temperature lift. *Nat. Energy* **5**, 996–1002 (2020).
9. Hawken, P. *Drawdown: the Most Comprehensive Plan Ever Proposed to Reverse Global Warming* 1st edn (Penguin, 2017).
10. Kitanovski, A. et al. in *Magnetocaloric Energy Conversion: From Theory to Applications* (eds Kitanovski, A. et al.) 97–166 (Springer, 2015).
11. Tušek, J. et al. A regenerative elastocaloric heat pump. *Nat. Energy* **1**, 16134 (2016).
12. Li, B. et al. Colossal barocaloric effects in plastic crystals. *Nature* **567**, 506–510 (2019).
13. Wang, R. et al. Torsional refrigeration by twisted, coiled, and supercoiled fibers. *Science* **366**, 216–221 (2019).
14. Zhang, T., Qian, X.-S., Gu, H., Hou, Y. & Zhang, Q. M. An electrocaloric refrigerator with direct solid to solid regeneration. *Appl. Phys. Lett.* **110**, 243503 (2017).
15. Defay, E. et al. Enhanced electrocaloric efficiency via energy recovery. *Nat. Commun.* **9**, 1827 (2018).
16. Chen, Y. et al. An all-scale hierarchical architecture induces colossal room-temperature electrocaloric effect at ultralow electric field in polymer nanocomposites. *Adv. Mater.* **32**, 1907927 (2020).
17. Neese, B. et al. Large electrocaloric effect in ferroelectric polymers near room temperature. *Science* **321**, 821–823 (2008).
18. Li, X. et al. Tunable temperature dependence of electrocaloric effect in ferroelectric relaxor poly(vinylidene fluoride-trifluoroethylene-chlorofluoroethylene terpolymer). *Appl. Phys. Lett.* **99**, 052907 (2011).
19. Zhang, G. et al. Ferroelectric polymer nanocomposites for room-temperature electrocaloric refrigeration. *Adv. Mater.* **27**, 1450–1454 (2015).
20. Klein, R. J., Xia, F., Zhang, Q. M. & Bauer, F. Influence of composition on relaxor ferroelectrics and electromechanical properties of poly(vinylidene fluoride-trifluoroethylene-chlorofluoroethylene). *J. Appl. Phys.* **97**, 094105 (2005).
21. Zhu, G. et al. Self-similar mesocrystals form via interface-driven nucleation and assembly. *Nature* **590**, 416–422 (2021).
22. Bai, G., Gao, D., Liu, Z., Zhou, X. & Wang, J. Probing the critical nucleus size for ice formation with graphene oxide nanosheets. *Nature* **576**, 437–441 (2019).
23. Meiners, T., Frolov, T., Rudd, R. E., Dehm, G. & Liebscher, C. H. Observations of grain-boundary phase transformations in an elemental metal. *Nature* **579**, 375–378 (2020).

24. Borgia, A. et al. Extreme disorder in an ultrahigh-affinity protein complex. *Nature* **555**, 61–66 (2018).
25. Jaffe, B., Cook, W. R. & Jaffe, H. L. *Piezoelectric Ceramics* (Academic, 1971).
26. Katsouras, I. et al. The negative piezoelectric effect of the ferroelectric polymer poly(vinylidene fluoride). *Nat. Mater.* **15**, 78–84 (2016).
27. Tan, S., Li, J., Gao, G., Li, H. & Zhang, Z. Synthesis of fluoropolymer containing tunable unsaturation by a controlled dehydrochlorination of P(VDF-co-CTFE) and its curing for high performance rubber applications. *J. Mater. Chem.* **22**, 18496–18504 (2012).
28. Le Gouplil, F. et al. Enhanced electrocaloric response of vinylidene fluoride-based polymers via one-step molecular engineering. *Adv. Funct. Mater.* **31**, 2007043 (2021).
29. Kessler, H. Detection of hindered rotation and inversion by NMR spectroscopy. *Angew. Chem. Int. Ed. Engl.* **9**, 219–235 (1970).
30. Hong, L. et al. Elastic and conformational softness of a globular protein. *Phys. Rev. Lett.* **110**, 028104 (2013).
31. Pirc, R., Kutnjak, Z., Blinc, R. & Zhang, Q. M. Upper bounds on the electrocaloric effect in polar solids. *Appl. Phys. Lett.* **98**, 021909 (2011).
32. Yang, L. et al. Novel polymer ferroelectric behavior via crystal isomorphism and the nanoconfinement effect. *Polymer* **54**, 1709–1728 (2013).

**Publisher's note** Springer Nature remains neutral with regard to jurisdictional claims in published maps and institutional affiliations.

© The Author(s), under exclusive licence to Springer Nature Limited 2021

# Article

## Methods

### Material synthesis

P(VDF-TrFE-CFE) with a composition of 65/35/7 mol% was purchased from Piezotech at Arkema. Triethylamine (water  $\leq$  50 ppm (by K.F.), 99.5%) and dimethyl sulfoxide-D6 (D, 99.8%, RG) were purchased from Adamas. The dehydrochlorination process of the terpolymer was carried out in a Schlenk tube under a dry nitrogen atmosphere at 50 °C in *N,N*-dimethylformamide (DMF) for a preset time. Specifically, triethylamine (1.5 ml, 10.7 mmol) was added to a solution of terpolymer (500 mg) in 6 ml of DMF under stirring in a nitrogen atmosphere at 50 °C and then reacted for 30–120 min. On cooling, the reaction mixture was dropped into a mixed solvent (100 ml) of water and ethanol (volume ratio of 1:1) to remove the residue. The resultant polymer was dissolved in 20 ml DMF followed by precipitation in an excess mixed solvent of water and ethanol three times<sup>33</sup> (see Supplementary Section 1 for more details).

### Polymer film preparation

The polymer films were prepared via solution-casting methods according to the literature<sup>18</sup>. The polymer powder was first dissolved in DMF (Sigma-Aldrich) at a concentration of 1.5 wt%. After vigorous stirring for 12 h, the solution was filtered through a glass fibre syringe filter with a pore size of 0.2 µm. The cast film was first dried at 60 °C for 8 h on a quartz plate, subsequently peeled off from the plates, and mounted on a homemade frame (stainless steel) for further annealing in a vacuum oven at 120 °C for 12 h. The typical thickness of the EC film was approximately 6 µm and could be tuned by varying the concentration of the solutions and the area of the plates. For all electric measurements, the Au electrodes were sputtered on the surfaces of the film, with a diameter of 6 mm for the upper electrode and 8 mm for the bottom electrode, unless otherwise specified (EMS Q150T ES Coater).

### Electrical and mechanical measurement

Temperature-dependent dielectric spectroscopy was performed via a Broadband Turnkey Dielectric Spectroscopy system (PolyK), equipped with an LCR meter (HP 4284A). The ambient temperature was controlled by a digitally controlled oven (EC1A Test Environment Chamber, Sun Electronics) equipped with a nitrogen tank. The temperature ramp was set to 0.5 K min<sup>-1</sup> from 100 Hz to 1 MHz. *P-E* loop measurements were conducted via a Polarization Loop & Dielectric Breakdown Test System (PolyK). The dielectric strength was tested by Shanghai Juter High Voltage Electrical & Equipment Co. under a d.c. voltage at a rate of 200 V s<sup>-1</sup>. The electrode diameter was 1 mm and the film thickness was 6 µm. Tensile mechanical testing was carried out on an Instron 5866 using a 200-N load cell and an extension rate of 10 mm min<sup>-1</sup> (see Supplementary Section 1.5).

### ECE measurement

ECE measurements were conducted in an in situ calibrated calorimeter, equipped with a heat flux sensor (27134-1, RdF Corporation). The high voltage was supplied by a Trek 610C high-voltage amplifier, and the signal was generated by an arbitrary function generator (Stanford Research Systems Model DS345). The results from the calorimeter were verified by an infrared camera. The infrared camera (FLIR A655sc) was fixed 30 cm above the EC film. The details of the measurement can be found in Supplementary Sections 1.6 and 1.7.

### Long-term cyclic measurement

The long-term cyclic experiments were conducted in a typical in-door laboratory at room temperature. The sample areas were fixed at 6 mm in diameter. Before the test, the ECEs were first recorded as the initial conditions. The films were then mounted on the ECE measurement setup, and cycled to directly visualize the EC cyclic performance. The frequency of the applied electric field was typically 0.5 or 1 Hz and

the maximum electric field was 50 MV m<sup>-1</sup> and 80 MV m<sup>-1</sup>. The signal of the heat flux sensor was displayed to monitor the condition of the film during the cycle. After the cycling, the films were tested for ECEs immediately.

### DSC

The latent heat of the phase transitions in the polymer was measured via the DSC 25 from TA Instruments. The samples were first cooled to –50 °C and cycled between –50 °C and 160 °C with a ramp rate of 20 °C min<sup>-1</sup>.

### WAXD and SAXS measurements

WAXD and SAXS characterizations were employed to monitor the structural evolution under electric fields at various length scales. The WAXD and SAXS measurements were carried out at the BL19U2 and BL16B1 beamline of the Shanghai Synchrotron Radiation Facility. The wavelength of the X-ray was 1.24 Å. Both two-dimensional (2D) WAXD and SAXS patterns were collected using a Pilatus 2M detector with a resolution of 1,475 pixels  $\times$  1,679 pixels and a pixel size of 172 µm  $\times$  172 µm. The data acquisition time for WAXD and SAXS was set as 15 s for each frame. The sample-to-detector distances of the WAXD and SAXS measurements were 207 mm and 2,030 mm, respectively. Details can be found in Supplementary Sections 1.12–1.14.

### Elastic incoherent neutron scattering

The elastic scattering intensity  $S(q, \Delta t) \approx I_{\text{inc}}(q, \Delta t) = \frac{1}{N} \sum_j b_j^2 \exp[-iq \cdot R_j(0)] \exp[iq \cdot R_j(\Delta t)]$  was normalized to the lowest temperature ( $\sim$  260 °C) and is approximately the value of the intermediate scattering function when decaying to the instrument resolution time,  $\Delta t$ , which is 1 ns for the HFBS instrument used. Here,  $q$  is the scattering wavevector,  $N$  is the total number of atoms,  $b_j$  is the incoherent scattering length of a given atom  $j$ , and  $R_j$  is the time-dependent position vector of atom  $j$ . All  $S(q, \Delta t)$  values were obtained in the temperature range of –260 °C to 80 °C during the heating process with the rate of 1.0 K min<sup>-1</sup> by using the HFBS at NIST<sup>34</sup>. Only the results from –20 °C to 80 °C are presented in Fig. 2f, as it is the temperature range most relevant to the function of the materials. The results were summed over the  $q$  from 0.45 to 1.75 Å<sup>-1</sup>.

### Estimation of the atomic MSD

The atomic MSD  $\langle X^2(\Delta t) \rangle$  was estimated by using a Gaussian approximation, where  $S(q, \Delta t) = \exp(-\frac{1}{6}q^2 \langle X^2(\Delta t) \rangle)$ . The values of  $q$  used for the Gaussian fitting ranged from 0.45 to 1.75 Å<sup>-1</sup>.

### Estimation of crystallinity and fraction of $\alpha$ and $\beta$ phases

The crystallinity was determined from 1D WAXD curves with the following formula:  $f_c = \frac{A_c}{A_c + A_a}$ , where  $A_c$  and  $A_a$  are the integration areas of the crystalline phase and the amorphous region, respectively. The fractions of  $\alpha$ - and  $\beta$ -crystalline forms in the total crystallites were determined by the following formulae:  $f_\alpha = \frac{A_\alpha}{A_\alpha + A_\beta}$  and  $f_\beta = \frac{A_\beta}{A_\alpha + A_\beta}$ , respectively.  $A_\alpha$  is the integration area of the  $\alpha$  phase and  $A_\beta$  is the integration area of the  $\beta$  phase.

### Estimation of crystallite size

The crystallite size was estimated by using the Scherrer equation:  $L_{hkl} = \frac{\lambda}{\beta \cos \theta}$ , where  $L_{hkl}$  is the crystallite size in the direction perpendicular to the  $(hkl)$  plane,  $\lambda$  is the X-ray wavelength,  $\theta$  is the Bragg angle and  $\beta$  is the line broadening at half the maximum intensity (FWHM)<sup>35,36</sup>. The dimensionless shape factor,  $K = 0.89$ , was used in this work.

### DFT calculation

The total energies of PVDF and P(VDF-DB) were calculated within the DFT framework by the software Quantum ESPRESSO and the ultrasoft pseudopotentials from the Standard Solid State Pseudopotentials (SSSP) library<sup>37</sup>. Cutoffs of 50 and 600 Rydberg (Ry) were used for the

wavefunction and charge density, respectively. The Monkhorst–Pack 2-4-4  $k$ -point mesh was chosen for the primitive PVDF unit cell and was modified for larger cells accordingly. We tested the vdW-DF functional, which did not improve the accuracy of structural parameters over the simpler PBE functional. Therefore, the PBE exchange-correlation functional was used. The atomic positions and cell parameters were relaxed with the energy convergence threshold 0.0001 Ry and force convergence threshold 0.001 Ry/ $a_0$ , where  $a_0$  is the Bohr radius (0.529 Å). See Supplementary Section 3 for more details.

## Device design and simulation

An all-solid, linearly oscillating cooling device model was built based on active EC regeneration. Numerical simulations were conducted using the commercial software COMSOL 5.5. The model was first calibrated with experimental results of a previously reported prototype<sup>4</sup>. Then the properties of the working bodies were substituted by those of the high-entropy polymer (TD-0.6%) reported in this work.

## Data availability

The datasets generated during and/or analysed during the current study are available from the corresponding authors on reasonable request.

## Code availability

Access to the phase-field model and DFT model codes are available on request from H.H. (hbhuang@bit.edu.cn) and J.B. (bernholc@ncsu.edu), respectively.

33. Yang, L. et al. Graphene enabled percolative nanocomposites with large electrocaloric efficient under low electric fields over a broad temperature range. *Nano Energy* **22**, 461–467 (2016).
34. Meyer, A., Dimeo, R. M., Gehring, P. M. & Neumann, D. A. The high-flux backscattering spectrometer at the NIST Center for Neutron Research. *Rev. Sci. Instrum.* **74**, 2759–2777 (2003).
35. Klug, H. P. & Alexander, L. E. *X-ray Diffraction Procedures for Polycrystalline and Amorphous Materials* 2nd edn (Wiley, 1974).
36. Tosaka, M. et al. Orientation and crystallization of natural rubber network as revealed by WAXD using synchrotron radiation. *Macromolecules* **37**, 3299–3309 (2004).
37. Ranjan, V., Nardelli, M. B. & Bernholc, J. Electric field induced phase transitions in polymers: a novel mechanism for high speed energy storage. *Phys. Rev. Lett.* **108**, 087802 (2012).
38. Chen, X. Z. et al. A nanocomposite approach to tailor electrocaloric effect in ferroelectric polymer. *Polymer* **54**, 5299–5302 (2013).

39. Lu, Y.-C. et al. Enhanced electrocaloric effect for refrigeration in lead-free polymer composite films with an optimal filler loading. *Appl. Phys. Lett.* **114**, 233901 (2019).

**Acknowledgements** This work was supported by the National Key R&D Program of China (2020YFA0711500 and 2020YFA0711503), the National Natural Science Foundation of China (52076127, 51776119, 11974239, 31630002, 51877132, 52003153 and 51972028), the Natural Science Foundation of Shanghai (20ZR1471700) and the China Postdoctoral Science Foundation-funded project 2019M661479. X.Q. acknowledges the support by the Prospective Research Program at Shanghai Jiao Tong University (19X160010008), the Oceanic Interdisciplinary Program of Shanghai Jiao Tong University (project number SL2020MS009), the Student Innovation Center and the Instrumental Analysis Center at Shanghai Jiao Tong University. X.C. and Q.M.Z. acknowledge the support of a seed grant from the Pennsylvania State University MRI-IEE, USA. L.-Q.C. acknowledges the support by the Donald W. Hamer Foundation through the Hamer professorship at Penn State. We thank L. Jiang and B. Zhu for assistance with measurements of energy-dispersive X-ray spectroscopy and attenuated total reflection Fourier-transform infrared spectroscopy. Access to the HFBS was provided by the Center for High Resolution Neutron Scattering, a partnership between the National Institute of Standards and Technology and the National Science Foundation under Agreement No. DMR-1508249. The DFT calculations were performed at the Oak Ridge Leadership Computing Facility, supported by DOE contract DE-AC05-00OR22725. We thank N. Li from the BL19U2 beamline, X. Miu from the BL16B1 beamline and Y. Yang at the BL14B beamline of Shanghai Synchrotron Radiation Facility for the help with synchrotron X-ray measurements. L.H. thanks the Innovation Program of the Shanghai Municipal Education Commission. H.Q. and J.B. thank B. Zhang and W. Lu for extensive discussions. X.Q. thanks S. Lin for support with simulation software, and X. Yao, Q. Wang and G. Meng for inspiring discussions. Certain commercial material suppliers are identified in this paper to foster understanding. Such identification does not imply recommendation or endorsement by the National Institute of Standards and Technology nor does it imply that the materials or equipment identified are necessarily the best available for the purpose.

**Author contributions** X.Q. conceived the concept, designed the experiment and wrote the manuscript. X.Q., D.H., Jie Chen, Q.L., F.D., X.H., S. Zheng and S. Zhang carried out the material synthesis and characterization. L.Z., D.H., Q.L., L.H. and X.Q. conducted the synchrotron X-ray measurements. L.Z. and M.T. conducted the neutron scattering tests. H.H. and X.S. carried out the phase-field simulation with guidance from L.-Q.C. H.Q. and J.B. carried out the DFT calculation. X.C. conducted the molecular mechanics simulation. X.Q. and D.H. designed the model for cooling devices. J.S. and Jiangping Chen supervised the device modelling. L.H. supervised synchrotron X-ray and neutron scattering tests. X.Q. and Q.M.Z. supervised the project. All authors analysed and interpreted the data.

**Competing interests** X.Q. and S. Zheng are inventors on a provisional patent application related to the described work. The other authors declare no competing interests.

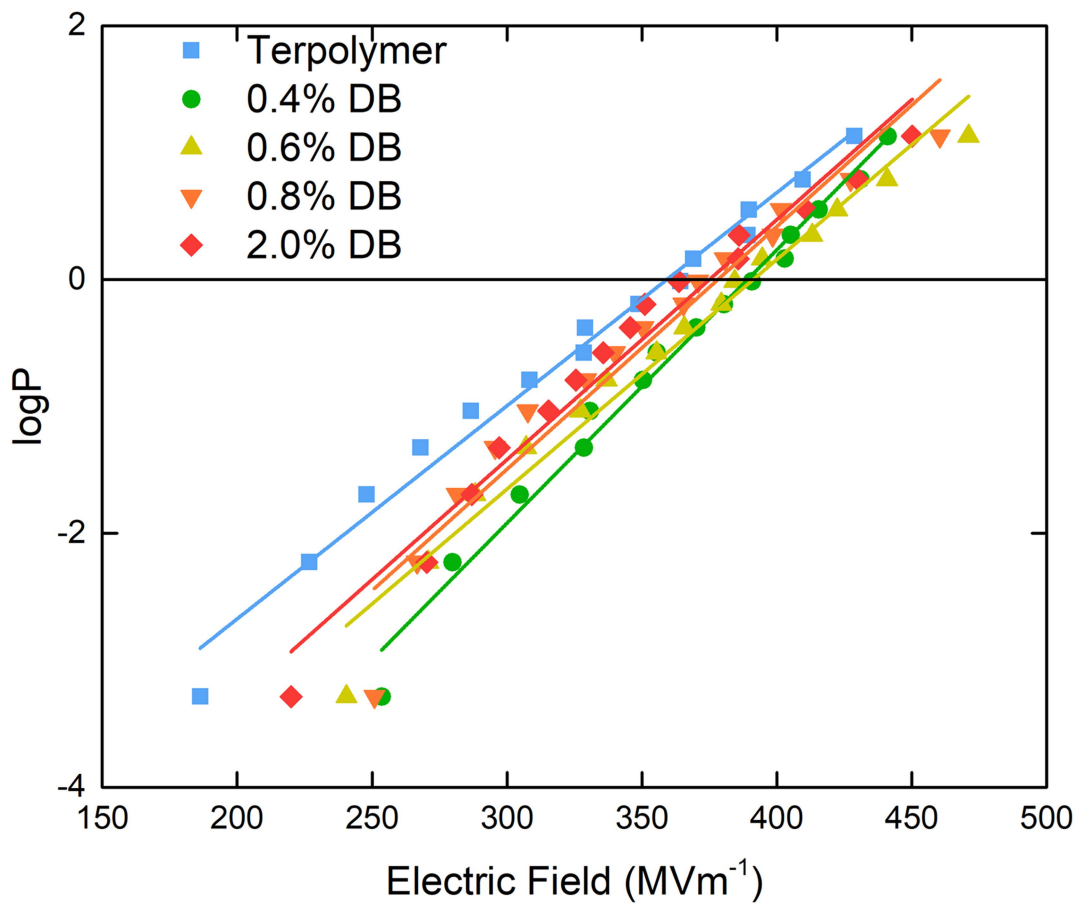
## Additional information

**Supplementary information** The online version contains supplementary material available at <https://doi.org/10.1038/s41586-021-04189-5>.

**Correspondence and requests for materials** should be addressed to Xiaoshi Qian, Xingyi Huang, Houbing Huang or Liang Hong.

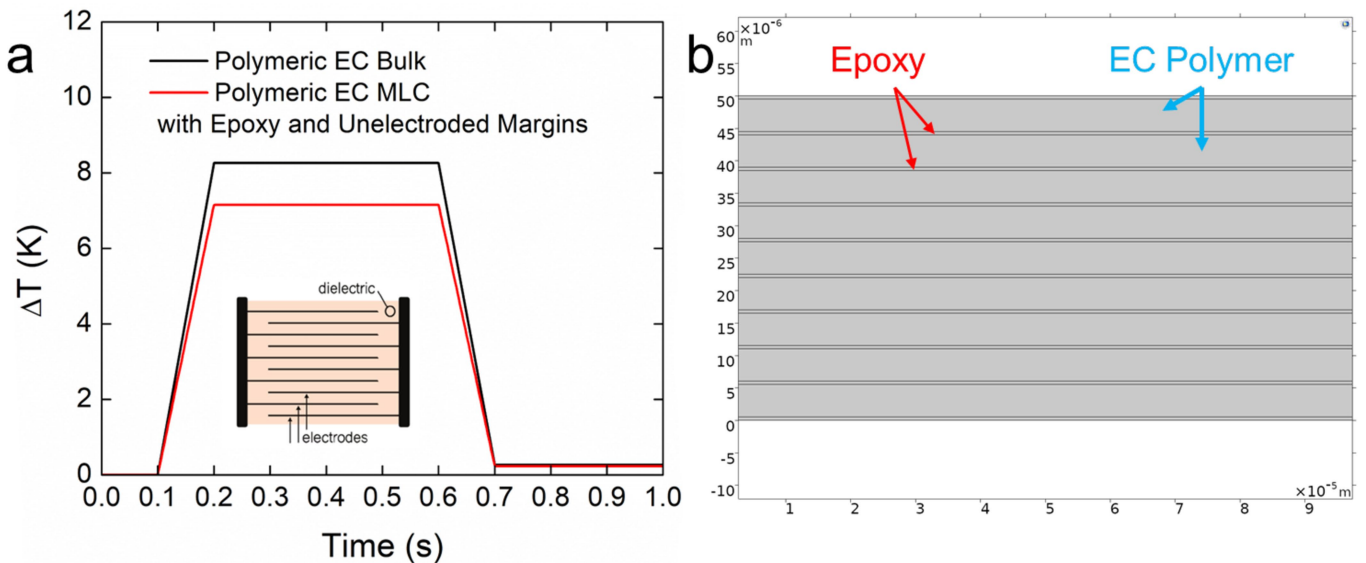
**Peer review information** *Nature* thanks Brahim Dkhil and the other, anonymous, reviewer(s) for their contribution to the peer review of this work.

**Reprints and permissions information** is available at <http://www.nature.com/reprints>.



**Extended Data Fig. 1 | Weibull plots of EC polymers with various -CH = CF- bond contents.** The breakdown strength was characterized at Shanghai Juter High Voltage Electrical & Equipment Co. Ltd. under a DC voltage at a rate of 200 V s<sup>-1</sup>. The electrode diameter was 1 mm and the film thickness was 6  $\mu$ m. After introducing 0.4 mol% of the double bonds, the Weibull breakdown

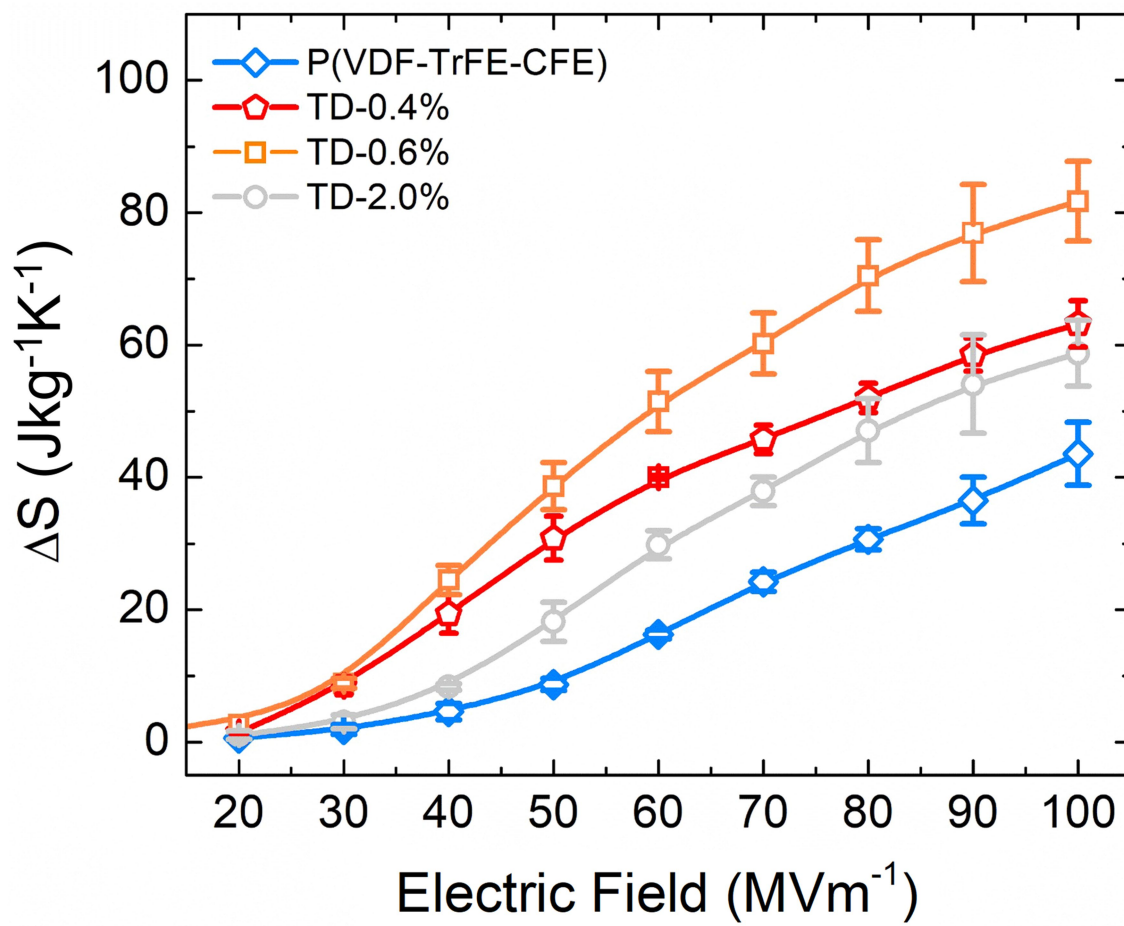
strength increased from 350 to 395 MVm<sup>-1</sup>. As the -CH = CF- bond content increased to 0.6%, 0.8%, and 2.0%, the Weibull breakdown strength decreased to 390, 375, and 370 MVm<sup>-1</sup>. As a result, the maximum cycling field can be extended to 80 MVm<sup>-1</sup> for TD-0.6%. 50 MVm<sup>-1</sup> is about 14% of the E<sub>b</sub> of the polymer.



**Extended Data Fig. 2 | Reduction of ECE in EC polymer MLC due to inactive materials.** a, Simulated temperature changes of the MLC with and without the epoxy (0.5  $\mu\text{m}$  thick) and un-electrode margin (with 1 cm  $\times$  2 cm total area and un-electroded margin = 0.5 mm on each side) as inactive materials.

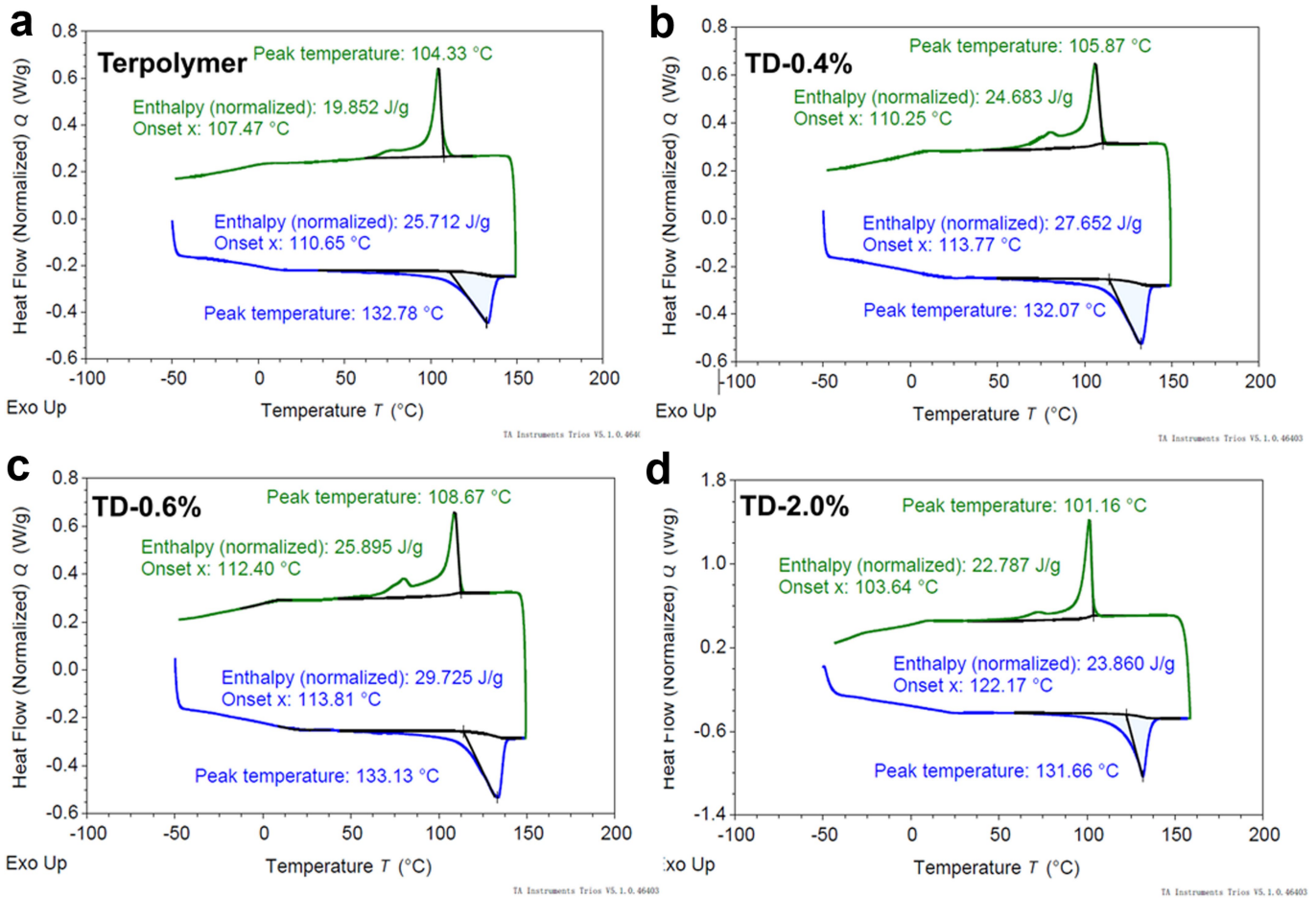
b, Schematics of the numerical model composing of 9 layers of EC polymer and

10 layer of epoxy. The electrode thickness for the polymer is below 0.05  $\mu\text{m}$  (negligible), and we considered the epoxy layer that mechanically stabilize the interfaces between each layers of MLCs. Hence, the total passive part in the MLC will be less than 15%, causing about 15% reduction of  $\Delta T$  (and  $\Delta S$ ).

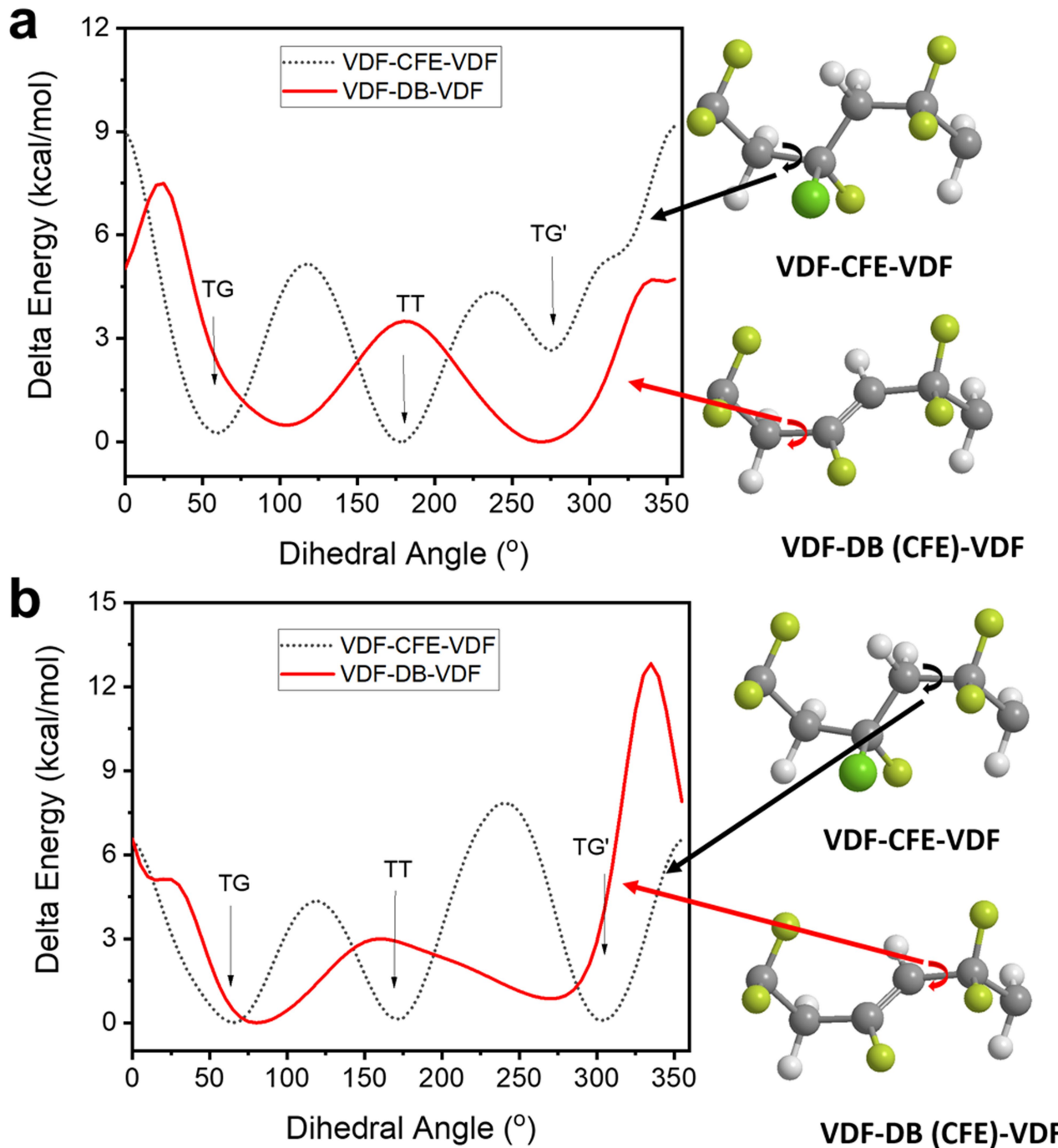


**Extended Data Fig. 3 | Field-dependent EC-induced entropy changes of the base terpolymer and the modified terpolymer with different mole percentages of CFE reduction.** EC-induced entropy changes of the base terpolymer and the modified terpolymers with different mole percentages of CFE reduction (*i.e.*, DB concentration ranges from 0, 0.4%, 0.6% and 2.0%).

( $n \geq 3$ , points are centred on the mean and the bars indicate the s.d., each sample of TD-0.6% in the EC heat flux measurement was verified by independent measurements by an infrared camera, see Supplementary Sections 1.6 and 1.7).



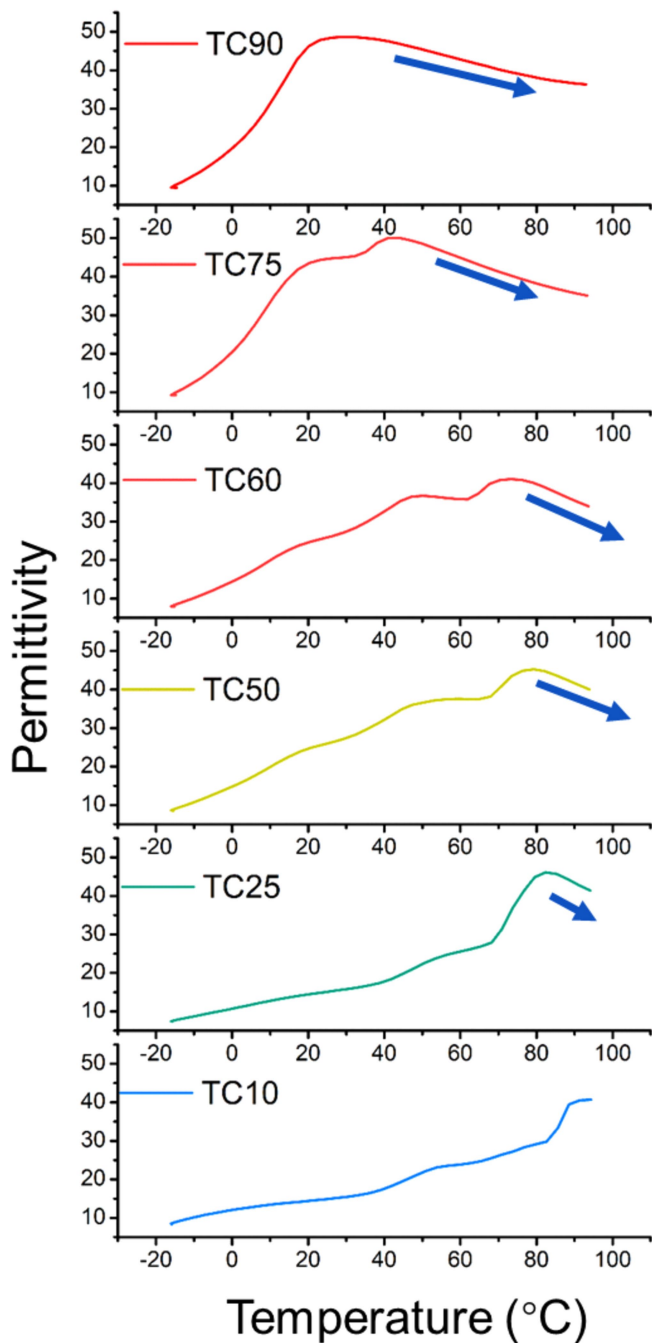
**Extended Data Fig. 4 | Heat flow signals of EC polymers during the heating and cooling process from the differential scanning calorimetry.** a, base terpolymer, b, TD-0.4%, c, TD-0.6% and d, TD-2.0%.



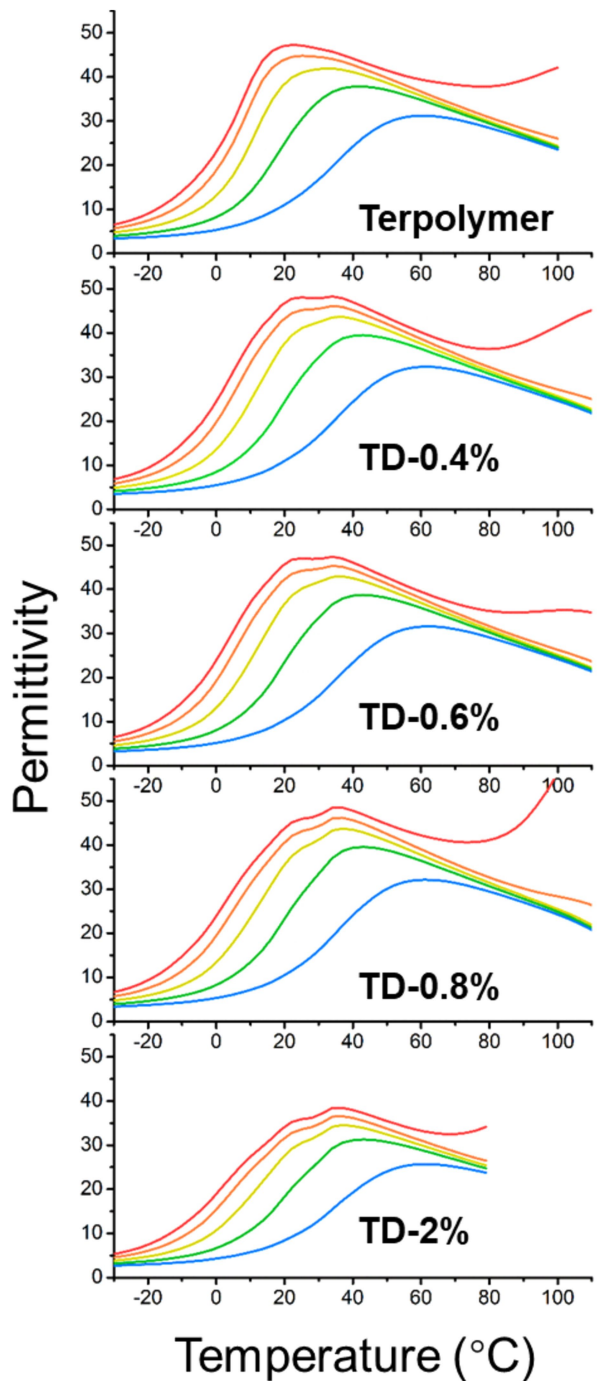
**Extended Data Fig. 5 | Rotation energy of carbon-carbon bond in PVDF single chains before (black) and after (red) a CFE group was replaced by a covalent double bond.** a, Rotation energy of the C-C bond adjacent to the Cl atom (on the left of the DB after the CFE reduction), and b, Rotation energy of the C-C bond on the other side of the CFE (DB) group. The simulation was

carried out by MM2 force field simulation through ChemOffice (version 19.0). The chain was defined as 5VDF + 1CFE + 5VDF and was relaxed in TGTG' conformation under zero kelvin. A covalent double bond was in-situ introduced by cancel a HCl of the CFE.

## Extrinsic blends



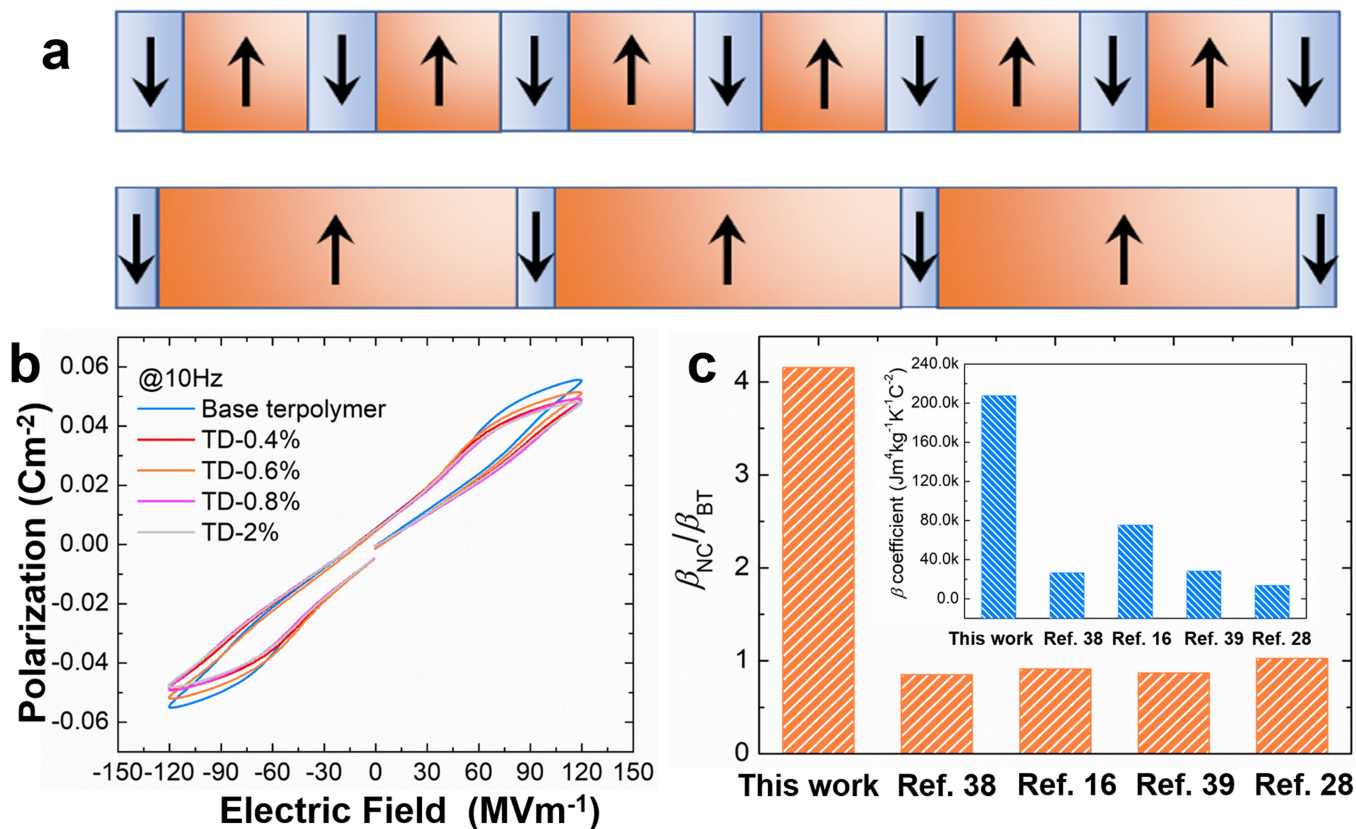
## Intrinsic modification



**Extended Data Fig. 6 | Comparison of the temperature-dependent permittivity between the extrinsic blends and intrinsically modified terpolymer.** The blends were composed of terpolymer P(VDF-TrFE-CFE) and copolymer P(VDF-TrFE) 65/35 mol%. The ferroelectric copolymer was intentionally added to generate a larger ECE by inducing internal fields and providing more polar entities. The composition of blends is noted as

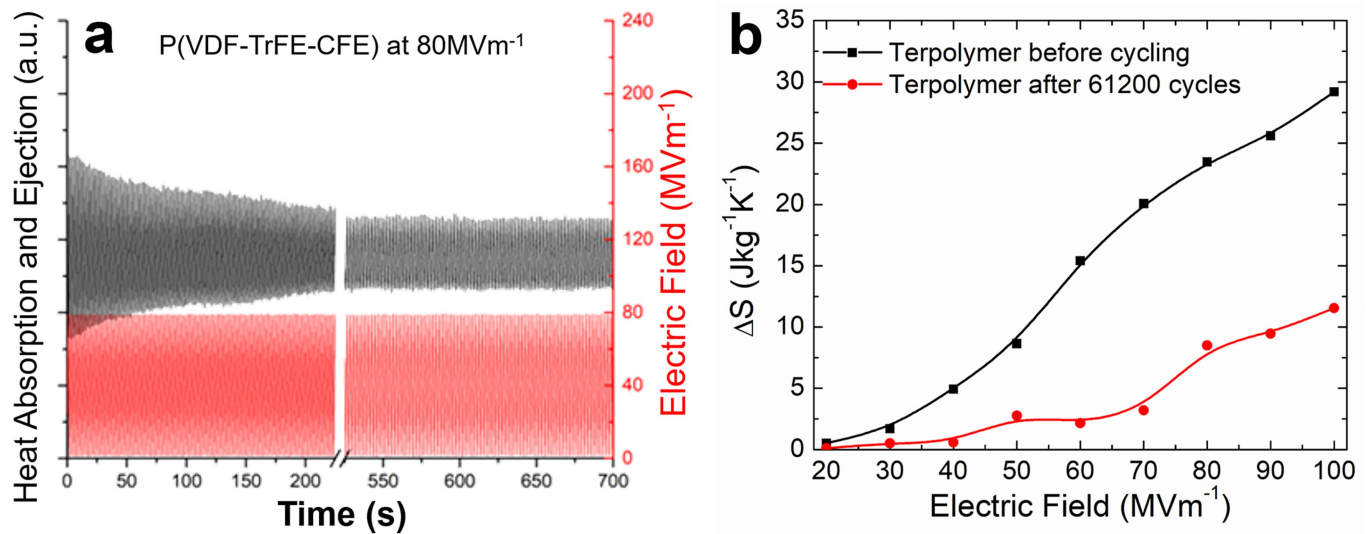
TC followed by the percentage of the terpolymer in the blends, e.g., TC90 refers to a polymer blend with 90 mol% terpolymer in the matrix. As the composition of ferroelectric copolymer increases, the dielectric material exhibits higher transition temperatures and stronger polar correlations as shown by the slope of blue arrows, compared with those of the TD series.

# Article



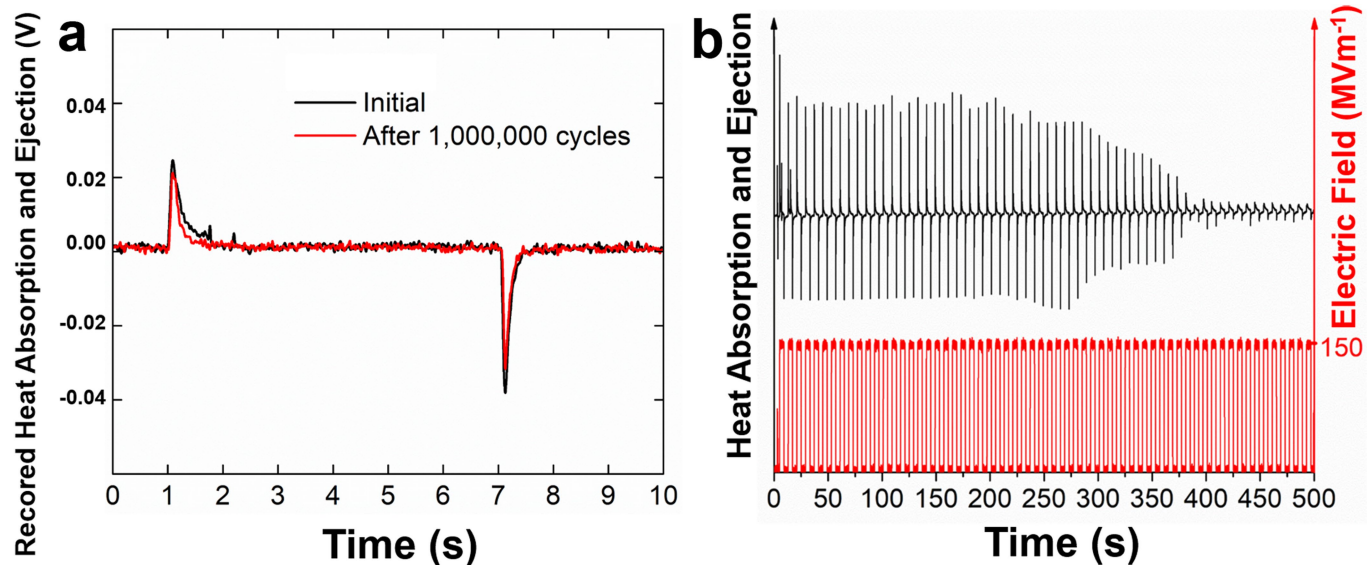
**Extended Data Fig. 7 | Relation between the maximum polarization and the electrocaloric effect of polar materials.** a, Schematic of microscopic ferroelectric-domain switching induced polarization change which does not generate electrocaloric effect. ECE is directly related to the electric field induced polarization change. In ferroelectrics and dielectric in general, the efficiency of inducing electrocaloric entropy change from polarization change can vary over a great range. As an example, macroscopic polarization domain switching, as illustrated here, although generates large polarization change, does not contribute to electrocaloric effect. b, Summarized P-E loops for the base terpolymer and TD series under  $120 \text{ MVm}^{-1}$  and  $10 \text{ Hz}$ . c, Ratio of the

$\beta$  coefficient of modified polymeric EC materials to their respective base polymers<sup>16,28,38,39</sup>, the inset presents values of the  $\beta$  coefficient of the enhanced EC polymeric materials reported in the literature and this work. As shown by Pirc *et al*<sup>31</sup>,  $\Delta S = P^2 \ln(\Omega)/(\epsilon_0 \Theta)$ , where  $\Omega$  is the number of polar entities (number of polar states) which can be accessed by dipoles,  $\epsilon_0$  is vacuum permittivity, and  $\Theta$  is an effective Curie constant, which is directly related to the polar correction in a ferroelectric material. Our results reveal that a large ECE can be achieved (at low fields) by engineering a high-entropy dielectric material which possesses a large  $\beta$  coefficient, and hence a large ECE may not require a material to have a large polarization.



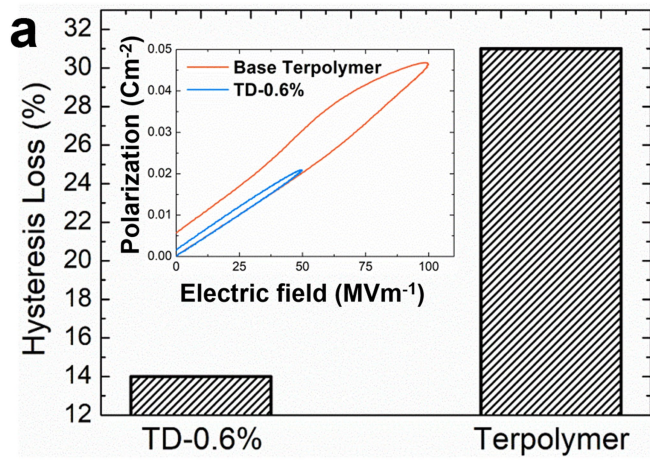
**Extended Data Fig. 8 | Fatigue behaviour of the base terpolymer P(VDF-TrFE-CFE).** a, In-situ heat flux directly recorded during cycling under  $80 \text{ MVm}^{-1}$ . b, Initially measured EC entropy change compared to that after 61200 cycles under different electric fields.

# Article

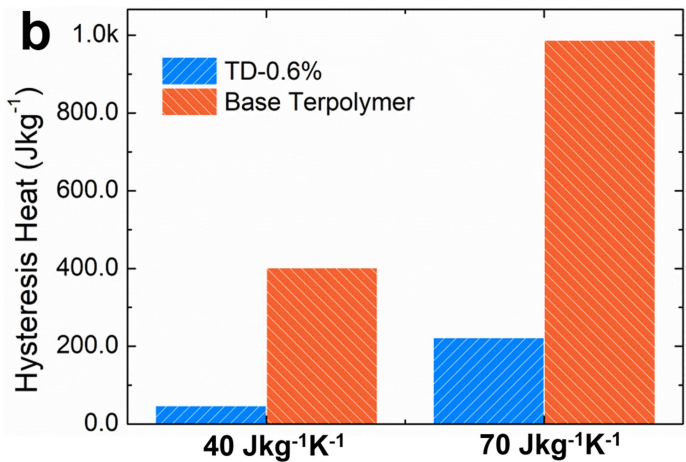


**Extended Data Fig. 9 | Comparison of the EC fatigue performances when the base terpolymer and the TD-0.6% were generating the same amount of ECE.**  
a, Cyclic performance of TD-0.6% before and after  $10^6$  cycles, at  $50 \text{ MVm}^{-1}$ .

The integrated peak areas, which represent the total heating and cooling signals, were similar to each other. b, The base terpolymer film experienced a series of breakdown after 50 cycles under  $150 \text{ MVm}^{-1}$ .



**Extended Data Fig. 10 | Comparison of hysteresis losses between the base terpolymer and the TD-0.6% high entropy polymer when they were generating the same amount of ECE.** a, Integrated hysteresis loss in percentage. The inset presents PE loops of the base terpolymer under



100  $\text{MVm}^{-1}$  and TD-0.6% under 50  $\text{MVm}^{-1}$ , at which the two polymers induced similar ECE. b, Hysteresis heat loss for the base terpolymer and TD-0.6% when they induce the same amount of entropy change of 40 and 70  $\text{Jkg}^{-1}\text{K}^{-1}$ , respectively.